The Birth of a Hawaiian Fissure Eruption

B.F. Houghton[1], C.M. Tisdale[1], E.W. Llewellin[2], J. Taddeucci[3], T.R. Orr[4], B.H. Walker[1], M.R. Patrick[5]

[1] Earth Sciences, University of Hawaii at Manoa, Honolulu, HI 96822, USA.

[2] Department of Earth Sciences, Durham University, Durham DH1 3LE, UK.

[3] Istituto Nazionale di Geofisica e Vulcanologia, Rome, Italy.

[4] Alaska Volcano Observatory, US Geological Survey, Anchorage, AK, 99508, USA.

[5] Hawaii Volcano Observatory, US Geological Survey, Hilo, HI 96720, USA.

Corresponding author: Bruce Houghton (bhought@soest.hawaii.edu)

Key Points:

- Eruption dynamics during a Hawaiian fountaining episode are tightly linked to patterns of rise and escape of large decoupled gas pockets.
- Variations in style are due to contrasting contributions of the decoupled gas pockets, and a coupled mixture of smaller bubbles and melt.
- Total in-flight mass is an effective proxy for intensity and provides an excellent record of pulsations in Hawaiian fountaining eruptions.

This article has been accepted for publication and undergone full peer review but has not been through the copyediting, typesetting, pagination and proofreading process, which may lead to differences between this version and the Version of Record. Please cite this article as doi: 10.1029/2020JB020903.

Abstract

Most basaltic explosive eruptions intensify abruptly, allowing little time to document processes at the start of eruption. One opportunity came with the initiation of activity from fissure 8 (F8) during the 2018 eruption on the lower East Rift Zone of Kīlauea, Hawaii. F8 erupted in four episodes. We recorded 28 minutes of high-definition video during a 51-minute period, capturing the onset of the second episode on 5 May. From the videos we were able to analyze the following in-flight parameters: frequency and duration of explosions; ejecta heights; pyroclast exit velocities; in-flight total mass and estimated mass eruption rates; and the in-flight total grain size distributions. Videos record a transition from initial pulsating outgassing, via spaced, but increasingly rapid, discrete explosions, to quasi-sustained, unsteady fountaining. This transition accompanied waxing intensity (mass flux) of the F8 eruption. We infer that all activity was driven by a combination of the ascent of a coupled mixture of small bubbles and melt, and the buoyant rise of decoupled gas slugs and/or pockets. The balance between these two types of concurrent flow determined the exact form of the eruptive activity at any point in time, and changes to their relative contributions drove the transition we observed at early F8. Qualitative observations of other Hawaiian fountains at Kīlauea suggest that this physical model may apply more generally. This study demonstrates the value of in-flight parameters derived from high resolution videos, which offer a rapid and highly time-sensitive alternative to measurements based on sampling of deposits post-eruption.

INDEX TERMS: 8428 Volcanology: Explosive volcanism; 8414 Volcanology: Eruption mechanisms,**;** 8434 Volcanology: Magma migration and fragmentation.

KEY WORDS: Physical volcanology, Kīlauea 2018 eruption, Basaltic explosive volcanism, Fissure eruptions, Eruption dynamics.

Plain Language Summary

We recorded the ‘birth’ of a ‘fountaining’ eruption of Kīlauea volcano on 5 May 2018, using a high resolution camera. The eruption passed from (1) pulsing escape of bursts of volcanic gas to (2) numerous close-spaced weak explosions ejecting particles torn from the magma (molten rock) in the vent, to (3) weak incandescent fountaining of particles and gas. Initially the behavior was dominated by meter-sized gas bubbles escaping freely through slow-rising magma beneath the vent. Rise of the magma and its mechanically coupled smaller bubbles played an increasing role with time and drove the switch to continuous fountaining. Observations of many earlier Kīlauea eruptions suggest that this model may apply generally to the initiation of this spectacular form of volcanic eruption.

1. Introduction

1.1. Basaltic Explosive Eruptions

Weak (or, 'mild') basaltic explosive eruptions are highly dynamic, showing shifts in style and particularly intensity on time scales of minutes to hours (e.g., Gurioli et al., 2008; Harris & Ripepe, 2007; Bani et al., 2013; Leduc et al., 2015; Gaudin et al., 2017). Fissure eruptions, a common feature at Kīlauea, Hawai'i, are invaluable observational settings to fill data gaps because, unlike single point-source vents, they often exhibit diverse styles and intensities over small time and length scales (e.g., Orr et al., 2015; Belousov et al., 2015; Witt et al., 2018). However, while eruption episodes at Kīlauea are emergent, the time scales of emergence are short, and they may reach peak intensity and height over just a few minutes to an hour (e.g., Richter et al., 1979). For this reason, there are no quantitative data for the initiation of fountaining episodes in Hawai'i. Qualitative records of the beginning (and end) of episodes often refer to initial intervals of low, discontinuous 'spattering' of ejecta (Richter et al., 1970; Swanson et al., 1979; Wolfe et al., 1988). We set out here, for the first time to constrain how a fountaining episode evolves from initial passive outgassing at a fissure, into sustained, pulsating fountaining.

1.2. The 2018 LERZ Eruption

In 2018, Kīlauea experienced a major flank eruption and summit caldera collapse (Neal et al., 2019). After a partial collapse at the Pu'u 'Ō'ō cone, on the middle East Rift Zone, on 30 April, magma propagated down-rift as a dike toward the more heavily populated lower East Rift Zone (LERZ). The first of 24 LERZ eruptive fissures (**Figure 1)** opened within the Leilani Estates subdivision just before 17:00 Hawaiian Standard Time (HST) on 3 May and significant activity ended on 4 August (Neal et al., 2019). The eruptive fissures during the first week of the LERZ eruption were up to several hundred meters long and episodes were generally not sustained on time scales longer than minutes to hours. Spatter cones/ramparts and lava pads accumulated adjacent to the fissures in early May but generally only within a few tens to hundreds of meters of the vents. At times up to six fissures were erupting simultaneously. Fissure 8 (F8) first erupted on 5 May with two short episodes lasting until 7 May.

Eruptive activity resumed at F8 on 27–28 May, discharging a lava flow to the north before stopping. F8 reactivated several hours later, and soon was the dominant source of discharge. F8 became the sole focus of eruption on 12 July, and remained so until the end of the fountaining on 4 August. Hawaiian fountains reached fluctuating heights of up to 80 m and fed a rapid channelized flow that ultimately entered the ocean 13 km down-flow, near the eastern tip of the island (Neal et al., 2019). This study focuses only on events at F8 between 20:32 and 21:12 on 5 May, during the first hour of the second episode.

1.3. Chronology of the Second Eruptive Episode at Fissure 8

The first two eruptive episodes at F8 were short-lived and occurred on 5–7 May, close to the start of the eruption. The first fountaining episode, which was not well observed, took place between approximately 10:40 and 14:00 HST on 5 May, and constructed a c. 0.7 to 1.0 m high spatter rampart, and a small tephra blanket. The second fountaining episode (**Figure 2** and **supplementary videos**) began eight hours later, at 20:32 on 5 May, from vents along a 10-12 m segment of the episode 1 fissure. The second episode continued through 6 May, as fountaining strengthened and propagated westward to define a final fissure some 90m long, generating the longest lava flow up until that point in the eruption (**Figure 1b)**. It had ended by 11:30 on 7 May, by which time 29 houses had been destroyed by lava flows from F8.

2. Approaches, Methods and Constraints on data

2.1. Framework for Observations

Our study uses high resolution video footage to quantify the changes in explosive activity across the fissure segment by measuring: 1) frequency and duration of explosions and pulses; 2) ejecta height; 3) pyroclast exit velocity; 4) in-flight total grain size distribution (TGSD), and 5) in-flight total mass and mass eruption rate (MER).

For convenience we define three principal phases of activity in the first hour of eruption (**Table 1**). Phase 1, which lacked pyroclasts, was not analyzed quantitatively. Different parameters proved useful for contrasting the activity in Phases 2 and 3. Durations of these phases and of the time intervals analyzed quantitatively are given in **Table 1**. Both have weaker initial and stronger subsequent periods which are described as 2A and 2B and 3A and 3B respectively.

2.2. Video Acquisition

We recorded the beginning of the second episode at F8 intermittently over a 51-minute period on the evening of 5 May, with the first recording starting at 20:21:04 and the last recording ending at 21:12:13. Approximately 28 minutes of footage was captured using a Sony Handycam FDR-AX100 camcorder filming at 30 frames per second (fps). Activity was recorded at a cluster of closely spaced vents along a c. 4-meter portion at the western extremity of the fissure segment. Eruption from a second cluster of generally weaker vents to the east was also sporadically recorded, but is not analyzed here. Advancing ‘a‘ā lava from the base of the fissure forced us to shift position regularly, so that the field of view becomes progressively larger in each subsequent video. This, and the dynamics of the eruptive conditions, make exact correlation of vents difficult. In the absence of a laser range finder, scales were calibrated by measuring pixel count for objects (see **Supporting Information**) of known length or diameter in, or close to, the plane of the fissure. Pixel size ranged from 2 to 8 mm.

2.3. Video Analysis

In-flight eruption parameters were analyzed for 2A and 2B from 90 second clips and 3A and 3B for 45 second clips. In Phase 2 longer times were analyzed because of the lower frequency of explosions. At any time, 1–3 major vents were active along the fissure segment. We adopt the convention of numbering the vents separately for Phases 2 and 3 in chronological order.

Maximum heights were determined in phase 2 by measuring the distance from the vent to the maximum height reached by the highest visible pyroclast. A small number of clasts were ejected out of our field of view; the maximum heights for these outlier clasts were estimated using exit velocity data. Pyroclast exit velocities were tracked manually in ImageJ, (a freeware software), using the MTrackJ plugin. Pyroclast trajectories were mapped from the vent for a minimum of 3 frames and a maximum of 6 frames, equivalent to 01. to 0.2 seconds. The time interval of tracking is necessarily short so that we can calculate average velocities before significant influence of gravitational deceleration. The scarcity of clasts present in Phase 2 allowed us to track most clasts, as long as they were visible in at least three frames. In Phase 3, because of the abundance of clasts, we tracked typically the 10 fastest clasts over time intervals of less than 1 second. Particle velocity can be influenced by secondary effects such as secondary fragmentation, particle–particle collisions (Vanderkluysen et al., 2012; Taddeucci et al., 2017), or local turbulence, and there can be confusion between overlapping and adjacent clasts, therefore we only present data for a pyroclast if the standard deviation of its individual measurements is less than 15%.

To calculate 'in-flight grain size' and 'in-flight total mass' we adapted an automated routine from Gaudin et al., (2014) that allowed us to measure all visible pyroclasts larger than -3.5 phi (11 mm) in a sequence of frames. Because of the uncertainties associated with low counts and small particle sizes in Phase 2 we only applied this method to Phase 3. The first step detects the pyroclasts in each frame across a stack of consecutive images. This is accomplished by enhancing the image contrast and then using an algorithm that determines which features are in motion and then removes the stationary background. The next step applies a threshold to the stack of images to isolate the clasts from the background. If necessary, the images are cropped to exclude any unwanted features that may be detected during the thresholding process. Clast area, perimeter, and the lengths of the major and minor axes are measured. The mass of each clast, in each frame, is estimated by multiplying the clast volume (calculated as the product of the clast area and its minimum Feret diameter) by an average density of 1100 kg m^{-3}, calculated from a sample of 100 measured pyroclasts from the early phases of the eruption (following Houghton and Walker 1989). The total mass in a frame is a conservative estimate of the total in-flight mass at that instant in time as some clasts are out of the field of view and others are obscured by adjacent clasts, incandescent gas, or features of the landscape. The 'in-flight grain size distribution' of the particles is summed in ½-phi bins, and median diameter and Inman sorting coefficient are calculated from the size data for each frame. Binning used the minimum Feret diameter of each clast. As a validation of the automated routine we also present data from two frames in Phase 3 in which each clast was manually outlined and then measured using the same routine.

We also estimated in-flight MER. This was done using a similar approach to the total mass determination, but rather than looking at the whole frame, we selected a small window above the vent, whose height was equivalent to the median clast diameter for that phase. This approach minimizes the possibility of interference from counting clasts multiple times but some smaller clasts may still be counted twice and some larger clasts may extend beyond the upper and lower limits on the box. We counted particles as they pass through this box over sequences of 30 consecutive frames so that the aggregate mass of particles represented the flux over a time window of one second.

3. Terminology

We apply the term 'episode' to the period from the onset of strong pulsating outgassing at 20:32 on 5 May until the end of mass discharge at c. 11:30 on May 7. This c. 39-hour-long episode was preceded by a 9-hour gap in eruption at F8, and was followed by a 20-day hiatus in F8 activity (Neal et al., 2019). This use is thus consistent with the terminology applied to earlier Hawaiian fountaining eruptions (Figure 3), where widely spaced episodes each contain numerous short-lived pulses (Richter et al., 1970; Wolfe et al. 1988). We divided the first hour of this episode into three eruptive 'phases' of consistently different style and intensity All three phases of the eruptive episode were pulsatory in character, on sub-second to second timescales, even the early outgassing in Phase 1. The term 'pulse' has been applied to a range of explosive eruptive phenomena (e.g. Dominguez et al., 2016; Wolfe et al., 1988; Taddeucci et al., 2012a,b) and there is no consistent definition across this literature. Here, we use pulse to refer to the shortest fluctuations in eruption vigor, usually ranging from a fraction of a second to a few seconds in duration. A succession of pulses may form a single explosion, as observed in Phase 2 (this activity is rapid Strombolian, *sensu* Houghton et al., 2016), or a sequence of longer, stronger and more prolonged pulses, without appreciable repose intervals, may form a sustained but unsteady Hawaiian fountaining event, as observed in Phase 3.

4. Results

The intensities during the episode were always exceptionally low and there were no instantaneous shifts between styles. For these reasons we use simple descriptive terms like pulse and explosion in this section.

4.1. Qualitative description of activity

4.1.1. Description

Phase 1: Weak, continuous but pulsating outgassing, unaccompanied by ejection of pyroclasts, was taking place from the western end of the F8 fissure, when first observed at 16:00 hours. Three principal sites of gas jetting, visibly incandescent to heights of 0.2 to 1.3 m, were spaced along approximately 4 m of the fissure and rampart. Discharges at the three sites were somewhat synchronized in that new bursts of outgassing were frequently simultaneous, but often one or two sites would remain quiescent. By 19:00, stronger partially synchronized, pulsating incandescent outgassing was occurring from 3 to 5 point sources along this western end of the rampart.

Phase 2A: The pulsating outgassing increased in intensity, and, by 20:32, it was punctuated by pulsed ejection of clusters of up to 10 incandescent lapilli, to heights of <2 m from up to three vents (**Figure 2a**). The emission of pyroclasts was both sparse and infrequent at this stage. No pyroclasts were visible for c. 80% of the time, and two or more clasts were visible for only 5% of the time.

Phase 2B: The eruption built into more rapid and closely spaced but still discrete explosive activity. Pyroclasts were ejected to heights of up to 4 m (**Figure 2b**), in well-defined, pulsating explosions of often 100 or more pyroclasts.

Phase 3A: The activity became markedly stronger and semi-sustained but highly unsteady with time (i.e., we no longer recognized clear reposes) and was captured in video between 20:53:45 and 20:54:30 when first one, then two, vents showed quasi-sustained, but pulsating, ejection of coarse lapilli and bombs (**Figure 2c**) typically to 10 to 20 m height. Pulses were maintained for intervals of several seconds, with any pauses generally less than 1 s duration.

Phase 3B: Activity from the two principal vents (vents 1, 2) was sustained for tens of seconds and noticeably more intense than in 3A with rare outlier clasts rising to 50 m (**Figure 2d**), but was still pulsatory, on time scales of seconds.

4.1.2. End of the episode

The field party returned to F8 at 21:55 when activity had temporarily weakened but it strengthened again to a major peak, from vents east of those studied here, in the early hours of 6 May, and the fissure extended further eastward to reach a final length of 90 m. The episode ended on the morning of 7 May.

4.2. Frequency and durations of pulses and explosions

Short-lived pulses are the most fundamental eruption units recognizable, despite different time scales, throughout Phases 2 and 3 (**Table 2**) and were also seen in the pulsating nature of outgassing in Phase 1. The latter were not documented in this study.

4.2.1. Results

Phase 2A: We recorded 150 pulses from the strongest vent over 4 minutes of filming, with durations ranging from 0.07 to 2.4 seconds (**Table 2)**. This equates to a pulse frequency of 0.6 s^{-1}. The pulses show a tight log-normal distribution about a mean value of 0.41 seconds (**Figure 4**). We group the pulses into 36 explosions, some of which consist of a single isolated pulse, others consist of multiple pulses within a single explosion. Explosion duration ranges from 0.19 to 11.7 seconds without a single well-defined mode and a periodicity of 7 seconds. Repose intervals between explosions range from 0.6 to 18.5 seconds.

Phase 2B: We recorded 166 pulses in a 92 second video clip, with durations ranging from 0.1 to 2.2 seconds, with a tight lognormal distribution about a mean of 0.41 seconds (**Figure 4**) and a pulse frequency of 1.8 s^{-1}. The pulses were grouped into 12 explosions ranging in duration from 0.17 to 21.6 second. Like 2A, these is no single mode for the event durations and there are insufficient explosions to calculate meaningful statistics, although the period is approximately 8 seconds. Repose intervals between explosions range from 0.7 to 2.2 seconds.

Phase 3A: There are no significant reposes during 3A and hence no recognizable explosions. The eruption does however pulsate, as is clear in the time series shown later in **Figure 8**. Ten pulses were recorded in 45 seconds of filming with durations from 1.8 to 7.2 seconds (**Table 2, Figure 4**).

Phase 3B: We recorded 59 pulses during 270 seconds of filming with a range of 1.9 to 10.2 s.

4.2.2. Interpretation

Analysis of the data presented in **Figure 4** shows that the durations of pulses are statistically indistinguishable between Phases 2A and 2B (ANOVA p-value = 0.929) and between Phases 3A and 3B (ANOVA p-value = 0.752). In the case of Phase 2, this holds despite a 3-fold increase in the frequency of pulses from 2A to 2B. The durations of pulses in Phase 2 are statistically significantly different from those in Phase 3 (ANOVA p-value = 0.000). This suggests that there is some fundamental property of the system that tightly modulated the duration of pulses within each phase, and which changed rapidly between Phases 2 and 3. This is mirrored in the in-flight data described below. No similar pattern is observed in event duration.

4.3. Pyroclast Velocimetry

The exit velocities of pyroclasts (**Figure 5**) show a consistent and predictable pattern of increase as the eruption increases in intensity. We recorded the pyroclasts associated with each of the three vents separately in 2B. In Phase 3 we tracked two dominant vents, other minor vents were active intermittently.

4.3.1. Results

Phase 2A: The few pyroclasts emitted in 2A showed consistently the lowest pyroclast exit velocities. These pyroclasts decelerated sharply on ejection and were rapidly advected by the near-surface wind. The majority of measured pyroclasts across all three vents during this phase had exit velocities of 3–9 m s^{-1} (**Table 2)**. The velocities were consistently highest at vent 2 and lowest at vent 3.

Phase 2B: There was a significant increase in average velocity with respect to 2A (**Table 2**), but little change with time throughout 2B. The average velocity was 8 m s^{-1} and the maximum 15 m s^{-1} (**Figure**

5a). The data show that the activity at all 3 vents generally overlapped, even though the exit velocities were not identical. The onset of explosions at vent 3 was often slightly delayed with respect to 1 and 2, and vent 3 exit velocities were consistently low (mostly 3–8 m s^{-1}, average 5.6 m s^{-1}). Velocities at vent 1 and vent 2 were more typically 7–12 m s^{-1}, averaging 8.1 and 7.6 m s^{-1} respectively. A non-linear decay of ejection velocity signaled the end of well-defined ejection pulses.

Phase 3: The onset of Phase 3 was marked by a rapid increase in the number of fast moving particles. As a consequence, very few slow-moving clasts (3–5 m s^{-1}) were recorded and exit velocities clustered at 15–20 m s^{-1} (**Figures 5b, c**). The average velocity was 18 m s^{-1} for both 3A and 3B, with maximum velocities of 34 and 35 m s^{-1} respectively (**Table 2**). Vent 2 emerged with relatively low velocities at 30 s into 3A but from 37 s vent 2 velocity essentially matched that of vent 1.

4.3.2. Interpretation

All measured exit velocities are low by comparison to Strombolian eruptions; e.g., exit velocities across nine studies of normal explosions at Stromboli, complied by Bombrun et al., (2015), have mean values of 22–136 m s^{-1}. Taddeucci et al., (2012b) recorded ranges of 38–149 m s^{-1} and 172–405 m s^{-1} for mean and maximum velocities respectively for six normal explosions on Stromboli in 2009. There are no comparative exit velocities for other Hawaiian eruptions at Kīlauea, although exit velocities of up to 100 m s^{-1} can be estimated for fountains reaching to heights of 100 m.

As expected, exit velocity increased from Phase 2 to Phase 3 as the eruption became more sustained. We discuss relationships between exit velocity and the other parameters in later sections.

4.4. In-flight Total Grain Size

4.4.1. Results

Phase 2: The small number and fine size of pyroclasts in single frames from the Phase 2 footage prevented us from calculating meaningful in-flight TGSD, but pyroclast sizes were typically 1–4 cm.

Phase 3: Consistent TGSDs within single video clips were observed during Phase 3. For validation, we hand-drew outlines and measured pyroclasts in two frames from 3A and four frames from 3B (**Figure 6; Supporting Information)**. Automatically generated data and manually constrained data compare well (**Figure 6**).

For the automated data sets, median diameters range from 6 to 12 cm (-6.1 to -7.3 phi), in 3A (**Figure 7a**), increasing to 11 to 17 cm (-6.9 to -7.5 phi) in 3B (**Figure 7b**). All the data are very well sorted (**Figure 7c**), with Inman sorting coefficients of 0.5–0.8 phi (**Table 2**). The manual data are tightly clustered with median diameters of 10–11 cm and sorting coefficients of 0.7–0.8 phi.

Fluctuations in median diameter with time are shown in **Figure 8a, c**. There are significant temporal fluctuations in median diameter defining pulses for 3A (**Figure 8a**) and 3B (**Figure 8c**), which are matched closely by the in-flight mass data (**Figures 8b, 8d**) discussed below. Data points are color-coded based on the total number of clasts counted within each frame. There is no obvious correlation between clast counts and grain size for either 3A or 3B, reflecting that each image is a complex assemblage of both rising, and falling pyroclasts erupted at slightly different times.

4.5. In-flight Total Mass

4.5.1 Results.

We have calculated the total in-flight mass of pyroclasts in single frames, using a similar approach to the grain size analysis (**Figure 8b,d**).

Phase 2: In-flight mass values are very low in Phase 2 and seldom exceeded 1 kg. Values are subject to significant error for this reason (and due to the small particle diameter), so we have not analyzed footage from this time interval in detail.

Phase 3: In-flight mass values (**Table 2**) in 3A ranged from 20 to 800 kg (**Figure 8b**), and between 500 and 4100 kg in 3B (**Figure 8d**). The increase in the maximum in-flight mass and maximum clast counts with time across **Figure 8b** coincides with an observed rapid increase in the eruption rate. There is a strong positive correlation between in-flight mass and clast count, for both 3A and 3B.

4.5.2. Interpretation

In-flight eruptive mass defines pulses during Phase 3 exceptionally well (**Figures 8 b, d**) and corelates with MER. The three order-of-magnitude shift in observed in-flight eruptive mass between Phases 2 and 3 is fully consistent with a step-wise escalation and stabilization in the eruption that was observed over less than 1 minute at this point. A more gradual, one-order-of magnitude shift in erupted mass occurs between 3A and 3B (**Figures 2c, d**). A smaller progressive change is seen during 3A and marks both waxing of vent 1 and the addition of vent 2. Visual correlation of high clast numbers and high in-flight mass is strong and demonstrates that clast number is a strong influence on the value of in-flight mass and hence MER.

4.6. Estimates of MER and Eruption Intensity

4.6.1. Results

Phase 2: Our focus here has been on the sustained activity during Phase 3, but the approximate values arrived at for Phase 2 suggest very low MERs of less than 1 kg s^{-1}.

Phase 3: In 3A the minimum and maximum rates are 25 and 850 kg s^{-1}; minimum and maximum rates for 3B are 2000 and 8100 kg s^{-1} respectively. The change from 2B to 3A represents an upscaling of the eruption by almost three orders of magnitude over a minute.

4.6.2. Interpretation

It is difficult to make precise comparisons with MER values from other studies because these data are averaged over quite different, generally much longer, time scales, often over the entire duration of an explosion or an eruption episode. Nonetheless, these numbers would place the 2018 explosions as among the weakest documented basaltic eruptions. The currently documented weakest events, the 2008 explosive eruptions of Halemaʻumaʻu, Kīlauea (Houghton et al., 2013) also had MER values of 10^2–10^4 kg s^{-1}. Estimates of MER for five normal explosions at Stromboli in 2012, analyzed by Pioli & Harris (2019) are

7.4×10^3 to 6.5×10^4 kg s^{-1}. Strombolian paroxysms are two orders of magnitude higher, e.g., 2.1×10^6 kg s^{-1} (Pistolesi et al., 2011) and 1.1×10^7 kg s^{-1} (Rosi et al., 2006), and high Hawaiian fountains (e.g., **Figure 3)** have time-averaged discharge rates of 6×10^3 kg s^{-1} to 1.5×10^6 kg s^{-1} (Wolfe et al., 1988).

5. Discussion

5.1. Temporal Variability: Characteristic Frequencies of Activity

Patrick et al. (2019) propose two time scales for variations in MER based on observation of lava flows during the later stages of the 2018 eruption. The first time scale is sporadic or intermittent pulsating in lava discharge on a timescale of 5 to 10 minutes. The second is longer term surges of effusion rate, on a timescale of 25 to 50 hours, driven by pressure changes triggered by small-scale collapse events at the Kīlauea summit. Patrick et al. relate the first to changes in the efficiency of outgassing at the vent.

Our in-flight parameters suggest there are at least two shorter timescales (higher frequencies) during, at least, the first 2 days of the eruption. The first are short-lived pulses in MER, with a periodicity of 0.6 to 4.5 seconds, linked to increases in both pyroclast counts and in-flight total grain size (**Figure 7**). These occurred throughout this early F8 episode, and at most of the other earlier eruptive fissures. The second are explosions, with closely spaced pulses, with periodicities of 5 to 8 seconds, seen during Phase 2 of the episode. We have witnessed this behavior also at other 2018 vents, noticeably the western end of fissure 17. We infer that the shorter time scale (pulses) reflect the bursting of individual large bubbles through the free surface of the magma. We interpret the longer explosions in Phase 2 as linked to the spaced arrival of larger, ordered gas pockets, representing tightly grouped clusters of such large bubbles.

It is important to note that all three shorter term fluctuations seen during the 2018 eruption (the short term pulsations in lava effusion (Patrick et al., 2019) and our pulses and explosions) are not driven by short-lived shifts in magma supply rate. Rather they show the importance of the frequency and timing of decoupled gas pockets in influencing style and frequency of eruption.

5.2. Spatial Variability: Connectivity and Synchronicity

There are three length scales operating along the fissure during the eruption, which must map to the patterns of fluid flow in the shallowest conduit (**Figure 9**). With increasing length scale there is, predictably, less evidence of connectivity and synchronicity of phenomena. The shortest is between adjacent vents within vent clusters like the one studied here on length scales of 1–3 meters. Vents in the studied cluster were generally in simultaneous eruption or repose, and the strongest explosions often begin in synchronicity at two or more vents. However, while pyroclast velocities are very consistent at any single vent, there are at times consistent differences between some vents. We suggest that this length scale reflects the dimensions of the largest decoupled gas pockets beneath the vent system. Because pockets consist of closely spaced large bubbles we propose that the variability between vents reflects the separation of the large bubbles, and their partitioning among the vents, at very shallow depths.

The intermediate length scale is the separation of vent clusters on single fissures. For early F8, the cluster that we have analyzed is 10 meters west of a second cluster of vents. This second cluster went into eruption after the western cluster and initially was significantly weaker (**Figure 9**). It switched from transient to semi-sustained eruption two minutes after the western cluster. Its intensity built, rivalling the western cluster at 21:00 and surpassing it by 22:00. These observations suggest that there is no direct connection between these clusters and we infer that the clusters are fed, at least at shallow levels, by independent trains of gas pockets (**Figure 9**). The localization of trains of ascending gas pockets may arise from in-conduit convection: Pioli et al (2017) found that focussed bubble trains form as part of along-strike convective cells in scaled analogue laboratory experiments within a dyke-like geometry.

On the longest length scale, of several hundred meters, there is no apparent connectivity in terms of the flux of large decompled gas pockets between adjacent fissures. There is also no pattern of consistent, down-rift opening of the fissure segments (F8 sits up-rift of F7 and down-rift of F9) which if present would have suggested that the melt phase ascended to the surface in a progressive fashion from west to east, down the rift zone. The eruptions of fissures may overlap partially in time but in a seemingly random pattern.

5.3. TGSD and Implications for Fragmentation Efficiency

Grain size measurements, and particularly total grain size distributions (TGSD), are key input parameters for studies of both magmatic fragmentation and for models of pyroclast transport and deposition. In explosive eruptions the available thermal energy is partitioned principally between fragmentation of the magma and its host rocks, and kinetic energy driving the dispersal of the pyroclasts.

TGSD remains the least quantified of source terms used in eruption models (e.g., Mastin et al., 2009). There are very few TGSD for Strombolian and Hawaiian products to compare with our data. Of twenty well constrained TGSD for fall deposits cited by Costa et al. (2016), only four are basaltic, none are Strombolian, and only two of these are from fountaining eruptions. A range of different techniques have been applied to these different deposits, so it is far from clear how compatible the datasets are. Furthermore TGSD can only be constrained from ground-sampling of pyroclast deposits on the scale of entire episodes or even complete eruptions; i.e., they represent very broad time-averages, of little use in constraining changing eruptive conditions during episodes or even extended eruptions. The only complete TGSD for a Hawaiian eruption remains the pioneering study of Parfitt (1998) for the 1959 Kīlauea Iki eruption which required assigning an extrapolated grain size distribution to the bulk of the ejecta which fell into the Kīlauea Iki lava lake. This result is a TGSD which is two phi units coarser than any other published data. It is also an average over a total of 16 fountaining episodes of widely varying height and intensity, although biased towards the final (relatively powerful) episodes. Nonetheless, its coarse grain size is consistent with the fact that 1959 was a significantly more powerful eruption than 2018, with fountaining to 580 m (Richter et al., 1970). Mueller at al. (2019) calculated GSD for two parts of the 1959 deposit but only used samples from the distal tephra blanket. These GSD are predictably significantly finer than either our data or those of Parfitt (1998). Analysis of the deposits of two fountaining eruptions at Mt Etna are also based on medial to distal samples and are similarly fine-grained (Costa et al., 2016).

The approach that we have adopted here has the advantage that the entire clast population > -3.5 phi (11 mm) is captured and little affected by the size and/or density fractionation that is seen in the final deposits of eruptions like Kīlauea Iki 1959 (Parfitt, 1998; Mueller et al., 2019). Other attempts at in-flight grain size determinations have been made for Strombolian explosions but not Hawaiian fountains. A variety of approaches have been previously applied to determining in-flight TGSD for Stromboli and Yasur (e.g., Gaudin et al., 2014; Bombrun et al., 2015; Pioli & Harris, 2019), mostly to video from infrared cameras. These show convincingly the shift in particle size and dynamics between single explosions but have a lower size limit set by the pixel resolution of the cameras (1.5-5 cm for these studies). Their data are averaged across the longer time frames of entire Strombolian explosions (duration 5 to 50 s) but still give very similar results to our work.

Our data show that, perhaps counter-intuitively, the TGSD of the eruption products coarsens from 3A to 3B. This suggests that the increasing eruption vigor leads to more widespread dispersal of the largest clasts and perhaps less efficient, rather than more efficient, primary fragmentation of the erupting melt.. Within Phase 3, there is also a positive correlation between eruptive mass and median diameter.

In Hawaiian and Strombolian eruptions unlike Plinian volcanism, the bulk of the erupted mass is represented by near-vent, coarse-grained material (cones and spatter ramparts). For example, for the Kīlauea Iki 1959 eruption, less than 2% of the erupted mass lies outside the 5 cm isopach (Klawonn et al., 2014). Thus, any grain size sampling that under-samples or ignores the often inaccessible and welded proximal products will greatly underestimate the TGSD, as suggested by Parfitt (1998). Our data and Parfitt’s (1998) research suggest that TGSDs for Strombolian and Hawaiian eruptions are both coarser grained and better sorted than could be implied from grain size distributions calculated from integrating the sets of single sieved samples found in the published literature (e.g., **Figure 7c**).

5.4. Relationship to Classical Strombolian and Hawaiian Styles

5.4.1. Current terminology

Two end-member styles of weak basaltic explosivity, Strombolian (Mercalli, 1881) and Hawaiian (Macdonald, 1972), have been recognized and universally adopted. The distinction lies primarily not in the magnitude of the explosions but instead in their duration (Houghton et al., 2016). Strombolian eruptions are typically successions of spaced, impulsive explosions (lasting seconds up to tens of seconds), whereas Hawaiian activity is characterized by emergent, sustained fountaining episodes frequently lasting hours to days. (e.g., Houghton & Gonnermann, 2008; Taddeucci et al., 2015). Typical average frequencies of 'normal' activity at Stromboli are 4 to 27 explosions per hour (Taddeucci et al., 2012a; Ripepe et al., 2008; Gaudin et al. 2017; Harris and Ripepe, 2007; Patrick et al., 2007). More recently, Houghton et al., (2016) introduced the term 'rapid Strombolian' to describe a variation on normal Strombolian activity, involving much more frequent explosions where the repose time between explosions approaches, or equals, the duration of the explosions. Examples include 3 explosions per minute seen at Villarrica in 2004 (Gurioli et al., 2008) and 7 explosions per minute at Etna in 2012 (Pering et al., 2015).

5.4.2. Phase 2

Phases 2A and 2B are both clearly characterized by spaced, transient explosions and both have a frequency of approximately 9 events per minute. They thus fit well with the few quantified examples of rapid Strombolian activity (e.g., Bertagnini et al., 1990, Gurioli et al., 2008; Pering et al., 2015).

5.4.3. Phase 3

Phase 3 does not readily fit into a conventional two-part Strombolian-Hawaiian classification (e.g., Walker 1973; Houghton et al., 2016). We suggest that it is a true hybrid between impulsive, transient explosivity and prolonged sustained fountaining, which is perhaps not unique, but has not previously been quantified. Similar behavior has been recognized at previous fissure eruptions in Hawaii (Swanson et al., 1979; Wolfe et al.,1998; Orr et al., 2015) and often informally termed 'spattering'– weak activity that is near-sustained, yet highly variable, and often linked to frequent bursting of large gas pockets.

5.5. How does a Sustained Fountain Begin?

This study is the first quantitative analysis of the start of a fissure-fed eruption episode at Kīlauea. The episode began with weakly pulsating emission of only outgassed magmatic volatiles from several vents over a 4-meter long length of a fissure formed earlier on the same day (Phase 1; **Figure 10a)**. We suggest that at this stage, the free surface of magma was below the ground surface, as a result of magma drawdown at the close of the earlier episode. This drawdown is likely to have opened up significant subterranean ‘head-space’ above the free surface (**Figure 10a)** into which decoupled gas pockets would have burst. In this model, any associated pyroclasts were intercepted by the shallow conduit walls and/or fell back into the conduit such that only gas reached the surface. This decoupled phase was a combination of gas from bubbles of all sizes that reached the free surface. The discharge of clearly decoupled magmatic gas remained a feature of the eruption even after near-continuous fountaining was established (**Figure 10c**).

As the flux of gas and melt increased with time, the free surface rose within the conduit (**Figure 10b**). The main eruption began with a phase of rapid discrete explosions in which initially only the smallest and fastest pyroclasts rose above the vent, to heights of a few meters (**Figure 10b**). We interpret pulses during this phase of the eruption as accompanying release of the largest and fastest moving, meter-sized gas bubbles, which were able to eject pyroclasts through any one of generally three vents. Eruptive pulses remained remarkably consistent in their duration during Phase 2, suggesting their dimensions were governed by the conduit geometry and a critical gas mass, that was required for rapid decoupled ascent, but their frequency increased three-fold from 2A to 2B, with both decreasing depth to the free surface and increased gas and magma fluxes. Pulses either occurred separately or grouped into explosions that often occurred synchronously across the vents typically 1–3 meters apart, suggesting a similar width for the maximum lateral extent of the gas pockets. However, synchronous explosions are not observed between this studied cluster of vents and a second cluster of vents approximately 6–10 meters to the west suggesting that outgassing proceeded independently on this longer length scale. Relatively low measured velocities at this stage reflect both the vigor of the subterranean bubble bursting and, probably more significantly, the fact that we are only seeing the upper portion of the trajectory of the pyroclasts, after substantial gravitational deceleration.

The relatively rapid transition into quasi-sustained but unsteady fountaining (Phase 3) was marked by a step-wise, 2–3 orders of magnitude increase in MER, a weaker coarsening of the pyroclasts, and a 2–3-fold increase in recorded pyroclast exit velocities. It is also the point at which the free surface of the magma is first seen at (then subsequently above) the previous ground surface. The gas pockets now burst at, or above, the previous ground surface and so the entire pyroclast population of each explosion is now visible. Higher velocities reflect both the increasing vigor of the explosions and the fact that we now tracked the full trajectory of the pyroclasts. Pulses were again driven by the bursting of large bubbles within gas pockets (**Figure 10c**) but we infer that significant volumes of smaller bubbles burst between each gas pocket ensured a near-continuum of clast discharge between peaks of mass discharge represented as the pulses.

5.6. A Qualitative Fluid Dynamic Model for the Eruptive Episode

Analog laboratory experiments conducted in an industrial or engineering context (e.g., Wallis, 1969; Clift et al., 1978; Taitel et al., 1980), have been essential to the development of our understanding of multi-phase fluid dynamics of basaltic explosive eruptions, despite some obvious contrasts (i.e. the higher viscosities, longer length scales, and lesser importance of surface tension in the latter). Early fluid-dynamic interpretations of basaltic explosive eruptions (e.g., Vergniolle and Jaupart, 1986, 1990) proposed that styles map to single regimes of multiphase flow seen in chemical engineering. Vergniolle and Jaupart (1986) and Parfitt and Wilson (1995) proposed buoyant ascent of decoupled slugs or gas pockets through largely stagnant melt to explain Strombolian explosions; in the case of Vergniolle and Jaupart (1986) an explicit analogy is made with bubble columns used in engineering laboratory experiments (Wallis, 1969; Taitel et al., 1980). Magma rise to form Hawaiian fountaining was interpreted in two contrasting ways as an analogy to either annular flow (e.g., Vergniolle and Jaupart, 1986; Jaupart and Vergniolle, 1988) or (coupled) bubbly flow (Parfit and Wilson, 1995; Parfitt, 2004). Seyfried and Freundt (2000) propose a finer subdivision of fountaining regimes into sporadic pulsating (single gas slugs), periodically pulsating (slug flow) and quasi-steady (annular).

Mudde and Saito (2001) consider the similarities in fluid dynamic behavior observed in laboratory experiments for bubble columns (buoyant rise of bubbles and gas slugs/pockets through stagnant fluid) and for air lift reactors (bubbly pipe flow in which there is bulk flow of the two-phase liquid driven by a pressure gradient along the pipe). They conclude that, in the general case, bubbly flow in a vertical pipe is essentially a superposition of the two processes. This means that, in an ascending column of liquid containing both small coupled bubbles, and large decoupled gas slugs/pockets, those two components can be considered independently: a gas slug rising through an ascending column of bubbly liquid behaves as it would in a stagnant column, but with an additional velocity component equal to that of the bubbly liquid through which it rises. We propose that, by analogy, these same two processes – the buoyant rise of meter-scale gas slugs and/or pockets, and the upward motion of the coupled mixture of smaller bubbles and melt – may operate simultaneously but somewhat independently across the range of Strombolian and Hawaiian activity seen at LERZ in 2018 and elsewhere. Although Mudde and Saito (2001) consider a cylindrical pipe geometry, the experiments of Pioli et al (2017) show that trains of bubbles and gas slugs/pockets are focussed into a column by convective flow in a slot, which would allow the same processes to operate in this dyke-like geometry. The superposition of these two types of concurrent flow at any point in time determines the exact form of the eruptive activity and changes to their relative contributions permits, for example, the transition into Phase 3, where significant volumes of smaller bubbles burst between each gas pocket, ensuring a quasi-sustained, near-continuum of clast discharge between pulses.

6. Conclusions

All aspects of eruption dynamics, across all styles at early F8, are tightly linked to patterns of rise and escape of large decoupled bubbles. Patterns of release of these gas pockets (rather than major but short-lived fluctuations of magma supply) drive variability of eruptive intensity and style on time scales of seconds to minutes and length scales of meters to tens of meters. Variations in activity can most easily be explained by contrasting contributions of the buoyant rise of meter-scale gas slugs and/or pockets, and the upward motion of a coupled mixture of smaller bubbles and melt, at different times and locations on the fissure. A progressive rise of the free surface of the magma was driven by changing gas and melt flux and in turn influenced the change with time in the form taken by the explosions, and promoted the transition to quasi-sustained fountaining. A positive feedback between flux and frequency of large bubbles and disturbance and subsequent behavior of the coupled population of the smaller bubbles in the surrounding melt assists in promoting sustained eruption.

In-flight TGSD offers a rapid, accurate, inclusive alternative to analysis and integration of hundreds of spot samples collected in the field. Total in-flight mass is both an effective proxy for MER and provides an excellent record of pulsations in fountaining eruptions.

Acknowledgements

This research was funded via NSF EAR 1829188, NERC NE/N018575/1, and funding from USGS via the disaster supplemental research program. Our work was supported by the US Geological Survey Volcano Science Center.We acknowledge the support and encouragement during this study and the scientific response to the 2018 from Christina Neal, who led us all so well. The authors would like to thank Carolyn Parcheta, Kyle Anderson, Alexa Van Eaton, Liliana Desmither, Patricia Nadeau, Michael Poland, and Michael Zoeller for discussions and suggestions during shared field time in 2018. The manuscript was significantly enhanced by reviews by Lis Gallant, Alexa Van Eaton and an anonymous reviewer. The authors have no financial conflicts of interest, or affliliations which might create a conflict of interest. The data used in this study is available at:

https://figshare.com/articles/media/The_Birth_of_a_Hawaiian_Fissure_Eruption_-_Supplementary_Videos/13315439?file=25656806

References

Bani, P., Harris, A.J.L., Shinohara, H., & Donnadieu, F. (2013). Magma dynamics feeding Yasur's explosive activity observed using thermal infrared remote sensing. *Geophysical Research Letters, 40*, 3830–3835. doi: 10.1002/grl.50722

Belousov, A., Belousova, M., Edwards, B., Volynets, A., & Melnikov, D. (2015). Overview of the precursors and dynamics of the 2012–13 basaltic fissure eruption of Tolbachik Volcano, Kamchatka, Russia. *Journal of Volcanology and Geothermal Research, 307*, 22–37.

Bertagnini, A., S Calvari, S., Coltelli, M., Landi, P., & Pompilio, M. (1990). Mount Etna: the 1989 eruption. *In* Mt Etna: the 1989 Eruption eds Barberi, F., Bertagnini, A., & Landi, P. (1990). Giardini, Pisa, 10–22.

Bombrun, M., Harris, A., Gurioli, L., Battaglia, J., & Barra, V. (2015). Anatomy of a Strombolian eruption: inferences from particle data recorded with thermal video. *Journal of Geophysical Research, 12*, 2367–2387. doi: 10.1002/(ISSN)2169-9356

Clift, R., Grace, J.R., & Weber, M.E. (1978). Bubbles, Drops and Particles. Academic Press, New York.

Costa, A., Pioli, L., & Bonadonna, C. (2016). Assessing tephra total grain-size distribution: Insights from field data analysis. *Earth and Planetary Science Letters, 443*, 90–107.

Dominguez, L., Pioli, L., Bonadonna, C., Connor, C.B., Andronico, D., Harris, A.J.L., & Ripepe, M. (2016). Quantifying unsteadiness and dynamics of pulsatory volcanic activity. *Earth and Planetary Science Letters, 444*, 160–168.

Gaudin, D., Taddeucci, J., Scarlato, P., Moroni, M., Freda, C., Gaeta, M., & Palladino, D.M. (2014). Pyroclast Tracking Velocimetry illuminates bomb ejection and explosion dynamics at Stromboli (Italy) and Yasur (Vanuatu) volcanoes. *Journal of Geophysical Research, 119*, 5384–5397. doi:10.1002/ 2014JB011096.

Gaudin, D., Taddeucci, J., Scarlato, P., Del Bello, E., Ricci, T., Orr, T.R., Houghton, B.F., Harris, A., Rao, A., & Bucco, A. (2017). Integrating puffing and explosions in a general scheme for Strombolian-style activity. *Journal of Geophysical Research, 122*, 1860–1875. doi:10.1002/2016JB013707

Gurioli, L., Harris, A.J.L., Houghton, B.F., Polacci, M., & Ripepe, M. (2008). Textural and geophysical characterization of explosive basaltic activity at Villarrica volcano. *Journal of Geophysical Research, 113*, B0820. doi:10.1029/2007JB005328

Harris, A., & Ripepe, M. (2007). Synergy of multiple geophysical approaches to unravel explosive eruption conduit and source dynamics— A case study from Stromboli. *Chemie der Erde, 67,* 1–35. doi:10.1016/j.chemer.2007.01.003

Houghton, B.F. & Carey, R.J. (2015). Pyroclastic fall deposits. In: Sigurdsson, H.; Houghton, B.F.; McNutt, S.; Rhymer, H.; Stix, J. (eds) *Encyclopaedia of Volcanoes,* 599-616 pp. Academic Press, San Diego.

Houghton, B.F., & Gonnermann, H.M. (2008). Basaltic explosive volcanism: Constraints from deposits and models. *Chemie der Erde Geochemistry, 68,* 117–140. doi:10.1016/j.chemer.2008.04.002

Houghton, B.F., Swanson, D.A., Rausch, J., Carey, R.J., Fagents, S.A., & Orr, T.R. (2013). Pushing the Volcanic Explosivity Index to its limit and beyond: Constraints from exceptionally weak explosive eruptions at Kīlauea in 2008. *Geology, 41,* 627–630. doi:10.1130/G34146.1

Houghton, B.F., Taddeucci, J., Andronico, D., Gonnermann, H.M., Pistolesi, M., Patrick, M.R., Orr, T.R., Swanson, D.A., Edmonds, M., Gaudin, D., Carey,R.J., & Scarlato, P. (2016). Stronger or longer: Discriminating between Hawaiian and Strombolian eruption styles. *Geology, 44,* 163-166. doi: 10.1130/G37423.1

Houghton, B.F. & Wilson, C.J.N. (1989). A vesicularity index for pyroclastic deposits. *Bulletin of Volcanology, 51*: 451-462. doi:10.1007/BF01078811

Jaupart, C., & Vergniolle, S. (1988). Laboratory models of Hawaiian and Strombolian eruptions. *Nature, 331*, 58-60. doi: 10.1038/331058a0.

Leduc, L., Gurioli, L., Harris, A., Colò, L., & Rose-Koga, E.F. (2015). Types and mechanisms of strombolian explosions: characterization of a gas-dominated explosion at Stromboli. *Bulletin of Volcanology, 77*, 1–15.

Mastin, L.G., Guffanti, M., Servranckx, R., Webley, P., Barsotti, S., Dean, K., Durant, A., Ewert, J.W., Neri, A., Rose, W.I., Schneider, D., Siebert, L., Stunder, B., Swanson, G., Tupper, A., Volentik, A., & Waythomas, C.F. (2009). A multidisciplinary effort to assign realistic source parameters to models of volcanic ash-cloud transport and dispersion during eruptions, *Journal of Volcanology and Geothermal Research*, *186*, 10–21. doi: 10.1016/j.jvolgeores.2009.01.008

Mercalli, G. (1881). Natura nelle eruzioni dello Stromboli ed in generale dell'attivita' sismico-vulcanica delle Isole Eolie. *Atti Societa` Italiana Scienze Naturali*, *24*, 105–134.

Macdonald, G.A. (1972). Volcanoes. Prentice-Hill, Eaglewood Cliffs, NJ.

Mudde, R.F., & Saito, T. (2001). Hydrodynamical similarities between bubble column and bubbly pipe flow. *Journal of Fluid Mechanics, 437*, 203–228.

Mueller, S.B., Houghton, B.F., Swanson, D.A., Poret, M., & Fagents, S.A. (2019). Total grain size distribution of an intense Hawaiian fountaining event: case study of the 1959 Kīlauea Iki eruption. *Bulletin of Volcanology, 81,* 43.

Neal, C.A., Brantley, S.R., Antolik, L., Babb, J., Burgess, M., Calles, K., Cappos, M., Chang, J.C., Conway, S., Desmither, L., Dotray, P., Elias, T., Fukunaga, P., Fuke, S., Johanson, I.A., Kamibayashi, K., Kauahikaua, J., Lee, R.L., Pekalib, S., Miklius, A., Million, W., Moniz, C.J., Nadeau, P.A., Okubo, P., Parcheta, C., Patrick, M.R., Shiro, B., Swanson, D.A., Tollett, W., Trusdell, F., Younger, E.F., Zoeller, M.H., Montgomery-Brown, E.K., Anderson, K.R., Poland, M.P., Ball, J., Bard, J., Coombs, M., Dietterich, H.R., Kern, C., Thelen, W.A., Cervelli, P.F., Orr, T., Houghton, B.F., Gansecki, C., Hazlett, R., Lundgren, P., Diefenbach, A.K., Lerner, A.H., Waite, G., Kelly, P., Clor, L., Werner, C., Mulliken, K., & Fisher, G. (2019). The 2018 rift eruption and summit collapse of Kīlauea Volcano. Science, *363*(6425), 367-374. doi: 10.1126/science.aav7046.

Orr, T.R., Poland, M.P., Patrick, M.R., Thelen, W.A., Sutton, J., Elias, T., Thornber, C.R., Parcheta, C., & Wooten, K.M. (2015). Kīlauea's 5–9 March 2011 Kamoamoa fissure eruption and its relation to 30+

years of activity from Puʻu ʻŌʻō. In Hawaiian Volcanoes: From Source to Surface. *American Geophysical Union Geophysical Monograph, 208,* 393–420.

Parfitt, E.A. (1998). A study of clast size distribution, ash deposition and fragmentation in a Hawaiian-style volcanic eruption. *Journal of Volcanology and Geothermal Research, 84,* 197–208.

Parfitt, E.A. (2004). A discussion of the mechanisms of explosive basaltic eruptions. *Journal of Volcanology and Geothermal Research, 134*, 77–107.

Parfitt, E.A., & Wilson, L. (1995). Explosive volcanic eruptions - IX. The transition between Hawaiian-style lava fountaining and Strombolian explosive activity. *Geophysical Journal International, 121*, 226–232. doi: 10.1111/j.1365-246X.1995.tb03523.x

Patrick, M.R., Dietterich, H.R., Lyons, J.J., Diefenbach, A.K., Parcheta, C., Anderson, K.R., Namiki, A., Sumita, I., Shiro, B., & Kauahikaua, J.P. (2019). Cyclic lava effusion during the 2018 eruption of Kīlauea Volcano. *Science, 366*, eaay9070. doi: 10.1126/science.aay9070

Patrick, M.R., Harris, A., Ripepe, M., Dehn, J., Rothery, D.A., & Calvari, S. (2007). Strombolian explosive styles and source conditions: Insights from thermal FLIR video. *Bulletin of Volcanology, 69*, 769–784. doi:10.1007/s00445-006-0107-0

Pering, T.D., Tamburello, G., McGonigle, A.J.S., Aiuppa, A., James, M.R., Lane, S.J., Sciotto, M., Cannata A., & Patanè D. (2015). Dynamics of mild strombolian activity on Mt. Etna. *Journal of Volcanology and Geothermal Research, 300,* 103–111. ISSN 0377-0273

Pioli, L., Azzopardi, B.J., Bonadonna, C., Brunet, M. & Kurokawa, A.K., (2017). Outgassing and eruption of basaltic magmas: The effect of conduit geometry. *Geology, 45*, 759–762.

Pioli, L., & Harris, A.J.L. (2019). Real-Time Geophysical Monitoring of Particle Size Distribution During Volcanic Explosions at Stromboli Volcano (Italy). *Frontiers in Earth Science.* https://doi.org/10.3389/feart.2019.00052

Pistolesi, M., Delle Donne, D., Pioli, L., Rosi, M., & Ripepe, M. (2011). The 15 March 2007 explosive crisis at Stromboli volcano, Italy: Assessing physical parameters through a multidisciplinary approach: *Journal of Geophysical Research, 116,* B12206. doi: 10.1029/2011JB008527

Richter, D.H., Eaton, J.P., Murata, K.J., Ault, W.U., & Krivoy, H.L. (1970). Chronological narrative of the 1959-1960 eruption of Kilauea Volcano, Hawaii. *U. S. Geological Survey Professional Paper 537-E,* l–73.

Ripepe, M., Donne, D.D., Harris, A., Marchetti, E., & Ulivieri, G. (2008). The Stromboli volcano: An integrated study of the 2002-2003 eruption. (2008), *American Geophysical Union Geophysical Monograph Series, 182*, 39–48.

Rosi, M., Bertagnini, A., Harris, A.J.L., Pioli, L., Pistolesi, M., & Ripepe, M. (2006). A case history of paroxysmal explosion at Stromboli: Timing and dynamics of the April 5, 2003 event. *Earth and Planetary Science Letters, 243,* 594– 606. doi:10.1016/j.epsl.2006.01.035

Seyfried, R., & Freundt, A. (2000). Experiments on conduit flow and eruption behavior of basaltic volcanic eruptions. *Journal of Geophysical Research, 105,* 23727–23740.

Swanson, D.A., Duffield, D.A., Jackson, D.B., & Peterson, D.W. (1979). Chronological narrative of the 1969-71 Mauna Ulu eruption of Kilauea Volcano, Hawaii. *U S Geological Survey Professional Paper* 1056.

Taddeucci, J., Alatorre-Ibargüengoitia, M.A., Moroni, M., Tornetta, L., Capponi,A., Scarlato, P., Dingwell, D.B., & De Rita, D. (2012a). Physical parameterization of Strombolian eruptions via experimentally-validated modeling of high-speed observations, *Geophysical Research Letters, 39*, L16306. doi:10.1029/2012GL052772.

Taddeucci, J., Scarlato, P., Capponi, A., Del Bello, E., Cimarelli,C., Palladino, D.M., & Kueppers, U. (2012b). High-speed imaging of Strombolian explosions: The ejection velocity of pyroclasts. *Geophysical Research Letters, 39L*, L02301. doi:10.1029/2011GL050404.

Taddeucci, J., Edmonds, M., Houghton, B.F., James, M.R., & Vergniolle, S. (2015). Hawaiian and Strombolian Eruptions. In: Sigurdsson, H.; Houghton, B.F.; McNutt, S.; Rhymer, H.; Stix, J. (eds) *Encyclopaedia of Volcanoes*, (pp. 485–504). Academic Press, San Diego.

Taddeucci, J., M. A. Alatorre-Ibargüengoitia, O. Cruz-Vázquez, E. DelBello, P. Scarlato, and T. Ricci (2017), In-flight dynamics of volcanic ballistic projectiles, *Rev. Geophys.*, 55, 675–718, doi:10.1002/2017RG00056

Taitel, Y., Barnea, D., & Dukler, A.E. (1980). Modeling flow pattern transitions for steady upward gas-liquid flow in vertical tubes. *American Institute of Chemical Engineering Journal, 26*, 345–54.

Vanderkluysen, L., A. Harris, K. Kelfoun, C. Bonadonna, and M. Ripepe (2012), Bombs behaving badly: Unexpected trajectories and cooling of volcanic projectiles, *Bull. Volcanol*., 74, 1849–1858, doi:10.1007/s00445-012-0635-8

Vergniolle, S., & Jaupart, C. (1986). Separated two-phase flow and basaltic eruptions. *Journal of Geophysical Research, 91*, 12842–12860.

Vergniolle, S. & Jaupart, C. (1990). Dynamics of degassing at Kilauea Volcano, Hawaii. *Journal of Geophysical Research*, 95, 2793–2809.

Walker, G.P.L. (1973). Explosive volcanic eruptions— A new classification scheme. *Geologische Rundschau, 62*, 431–446. doi:10.1007. /BF01840108

Wallis, G.B. (1969). One-Dimensional Two-Phase Flow: New York, McGraw-Hill, (pp. 410).

Witt, T., Walter, T.R., Müller, D., Guðmundsson, M.T., & Schöpa, A. (2018). The Relationship Between Lava Fountaining and Vent Morphology for the 2014–2015 Holuhraun Eruption, Iceland, Analyzed by

Video Monitoring and Topographic Mapping. *Frontiers in Earth Science.* https://doi.org/10.3389/feart.2018.00235

Wolfe, E.W. (1988). The Pu'u 'Ō'ō eruption of Kilauea Volcano, Hawaii: Episodes 1 through 20, January 3, 1983, through June 8, 1984. *United States Geological Survey Professional Paper, 1463*.

TABLES

Table 1: Recorded start and end times for Phases 1, 2 and 3 of the second episode of the F8 eruption (note the end time for Phase 3 is not known), plus estimates of their duration together, durations and start and end times for the analyzed videos. Video from Phase 1, which discharged only gas, was not quantitatively analyzed.

Phase	Start - End Time (HST) (Duration in min)	Time Analyzed (HST) (Duration)	Pixel Size (cm)	Phase Description
1	20:21:04 - 20:22:09 (0:01:05)	not analyzed	n/a	Pulsating outgassing from vents without accompanying pyroclasts.
2	20:32:17 - 20:52:01 (0:19:44)	2A: 20:32:17 - 20:33:47 (0:01:30) 2B: 20:47:43 - 20:49:13 (0:01:30)	2A: 0.16 2B: 0.26	Transient, impulsive explosive activity with pauses of up to 17 seconds.
3	20:54:13 - unknown (>0:18:00)	3A: 20:54:13 - 20:54:58 (0:00:45) 3B: 20:59:48 - 21:00:33 (0:00:45)	3A: 0.79 3B: 1.30	Continuous or near-continuous activity with no pauses longer than 1 second.

Table 2: Values of key eruption parameters calculated for stages of the early F8 eruption.

	Min	Max	Mean
Exit Velocity (m/s)			
2A	3	9	5
2B	3	15	8
3A	3	34	18
3B	5	35	18
Pulse Durations (s)			
2A	0.07	2.4	0.41
2B	0.1	2.2	0.41
3A	1.8	7.2	3.6
3B	1.9	10.2	4.5
Median Diameter (cm)			
3A	6	15	
3B	10	16	
Inman Sorting Coefficient (ϕ)			
3A	0.5	0.8	
3B	0.5	0.8	
Total Mass (kg)			
3A	10	850	
3B	500	4000	

Figure captions

Figure 1: Location map **(a)**. Map of the island of Hawaii. **(b)**. the lower portion of Puna district, with Leilani Estates subdivision, and the 2018 LERZ fissures. Fissures are numbered in chronological order following Neal et al., (2019). The entire 2018 flow field is in white (after Patrick et al., 2019). The early flow from fissure 8 as mapped on 8 May 2018 is shown in red.

Figure 2: Four images showing typical activity in phases 2 and 3 of the eruption: (**a)** 2A, (**b)** 2B, (**c)** 3A and (**d)** 3B. Hot pyroclasts appear bright white in color. Vents are labeled in red in chronological order. Red circles outline several of the sparse cm-sized ejecta in 2A and 2B. The images clearly reflect the increasing vigor of eruption and coarsening of the ejecta across the first hour of the episode. In each phase vents are numbered in order of chronological appearance.

Figure 3: Fountain height data from episodes 3 through 20 of the Puʻu ʻŌʻō eruption, (after Wolfe et al., 1988) to demonstrate the use of the terms eruption, episode/event and pulse.
(a) Plot of the frequency and duration of episodes 3–20. Heights for each bar are the maximum fountain height recorded during that episode.
(b) Detailed expansion of all fountain height data for episode 20 showing the emergent and then pulsating nature of the fountaining.

Figure 4: Box-and-whisker plots comparing log (duration in seconds) data for pulses during 2A, 2B, 3A and 3B. Note that, despite the wide range of values in each case, phases 2 and 3 are clearly statistically distinct.

Figure 5: Plot of pyroclast exit velocities versus time for: **(a)** 2B, **(b)** 3A, and **(c)** 3B. In (a) note the gaps without data which represent repose intervals between explosive events. Bars represent the standard deviation of measured velocities for any one pyroclast. In (**a**) note that consistently lower velocities are recorded at vent 3.

Figure 6: Comparison of grain size distributions for one frame from each of the 3A and 3B phases, derived using the automated and hand drawn approaches. **(a)** and **(d)** plot cumulative grain size distributions for 3A and 3B. Note in **(d)** the two curves almost coincide. **(b)** and **(e)** are histograms for the manual data with the clasts binned in ½ phi intervals. **(c)** and **(f)** present the automated data in the same fashion.

Figure 7: Plots of grain size data:

(a), (b) Median diameter vs Inman sorting for Phases 3A and 3B

(c) Plot of available median diameter versus sorting fields derived from sieve analysis of Strombolian and Hawaiian fall deposits (Houghton and Carey 2015). Green field is the sum of **(a)** and **(b),** i.e., all inflight TGSDs for Phase 3 of this study.

Figure 8:

(a), **(c)** Plots of median diameter versus time for 3A and 3B respectively, derived from analysis of pyroclasts captured in single frames. Data points are color coded for the number of clasts captured in each image. Note the contrasting scales due to the consistently higher number of clasts in 3B.

(b), (d) Plots of inflight total mass versus time for 3A and 3B respectively, derived from analysis of pyroclasts captured in single frames. Note the strong correlation in both plots of total mass and clast counts. Both sets of data show clearly the pulsating nature of Phase 3, and the escalation of activity from 3A to 3B.

Figure 9: Cartoon showing inferred relationship between eruption dynamics and subsurface flow of magma and a decoupled gas phase on contrasting length scales along a single fissure in 2018. Here we show two vent-clusters approximately 10 meters apart, which are essentially independent in terms of eruption frequency and intensity. Each cluster contains 3 or 4 vents, and these vents are often in simultaneous eruption and show correlations in eruptive intensity. Orange and white arrows indicate the relative flux of decoupled gas and magma respectively.

Figure 10: Cartoon showing progressive evolution of the eruption and subsurface flow in the shallow conduit for Phases 1, 2 and 3. **(a)** The magma-air free surface is below the ground surface in Phase 1 and only escaping decoupled gas reaches the surface. **(b)** In Phase 2, as the flux of gas and melt increase, the free surface rises, and the smallest pyroclasts are visible above the fissure. **(c)** A stepwise increase in eruption rate and pyroclast size occurs in Phase 3 and the free surface is now visible above the former ground surface. Pulses were again driven by the bursting of large bubbles within gas pockets but we infer that significant volumes of smaller bubbles burst between each gas pocket ensured a quasi-sustained, near-continuum of clast discharge between pulses. See Section 5.5 for detailed description. Orange and white arrows indicate the relative flux of decoupled gas and magma respectively. Width of field of view is approximately 4 m.

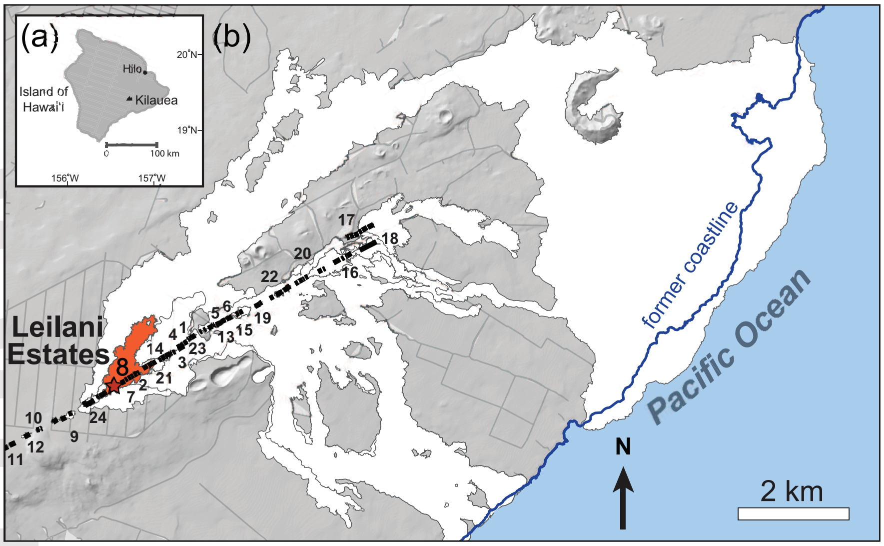

(a)
Island of Hawai'i
Hilo
Kilauea
20°N
19°N
0
100 km
156°W
157°W
(b)
Leilani Estates
former coastline
Pacific Ocean
N
2 km
1
2
3
4
5
6
7
8
9
10
11
12
13
14
15
16
17
18
19
20
21
22
23
24

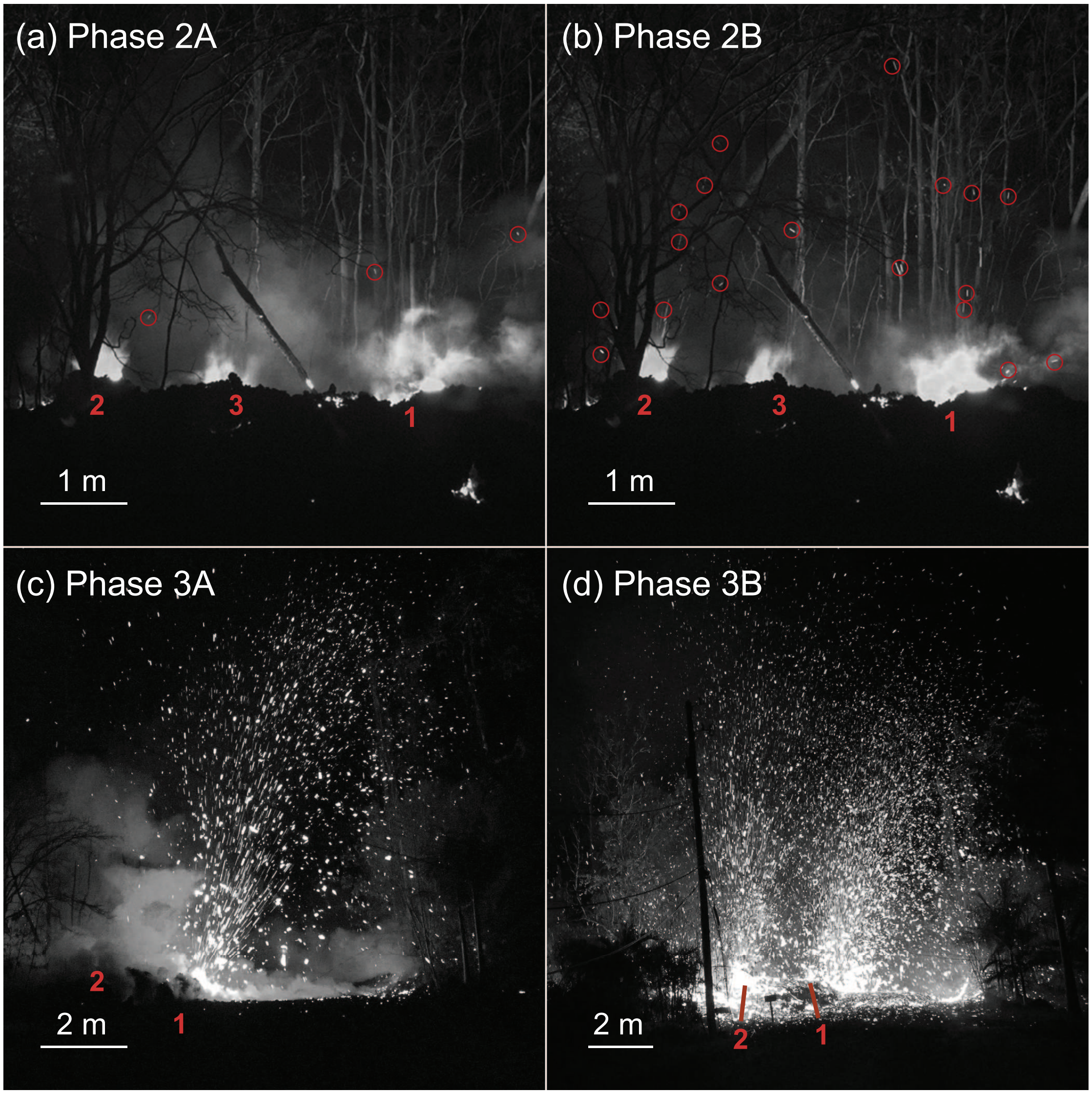
(a) Phase 2A
2
3
1
1 m
(b) Phase 2B
2
3
1
1 m
(c) Phase 3A
2
2 m
1
(d) Phase 3B
2 m
2
1

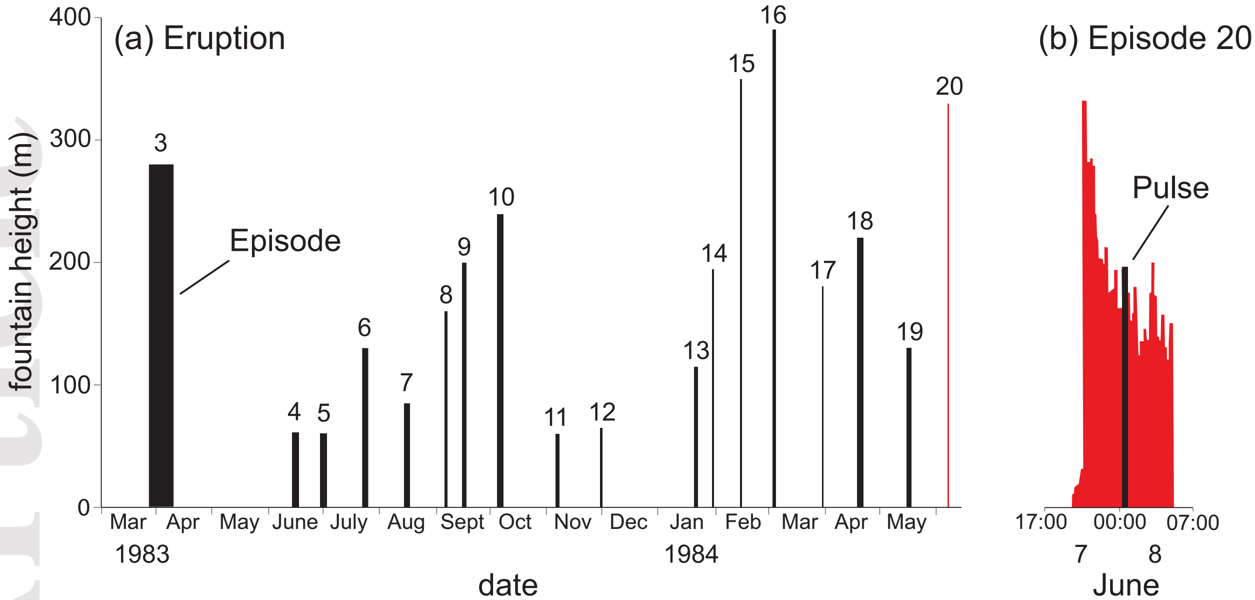

(a) Eruption
(b) Episode 20
400
300
200
100
0
fountain height (m)
3
Episode
4
5
6
7
8
9
10
11
12
13
14
15
16
17
18
19
20
Mar
Apr
May
June
July
Aug
Sept
Oct
Nov
Dec
Jan
Feb
Mar
Apr
May
1983
1984
date
Pulse
17:00
00:00
07:00
7
8
June

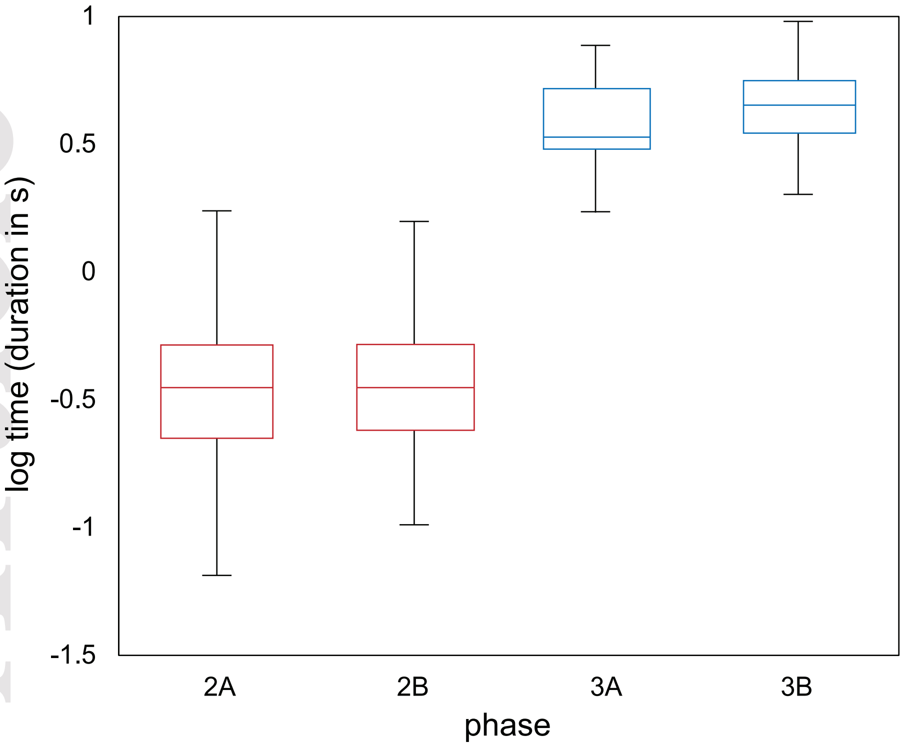
1
0.5
0
-0.5
-1
-1.5
log time (duration in s)
2A
2B
3A
3B
phase

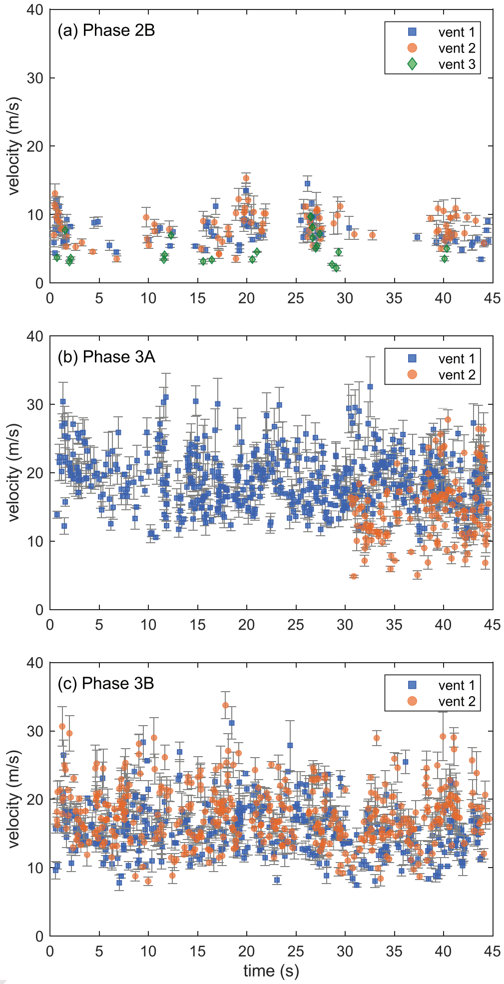

(a) Phase 2B
vent 1
vent 2
vent 3
velocity (m/s)
(b) Phase 3A
vent 1
vent 2
velocity (m/s)
(c) Phase 3B
vent 1
vent 2
velocity (m/s)
time (s)

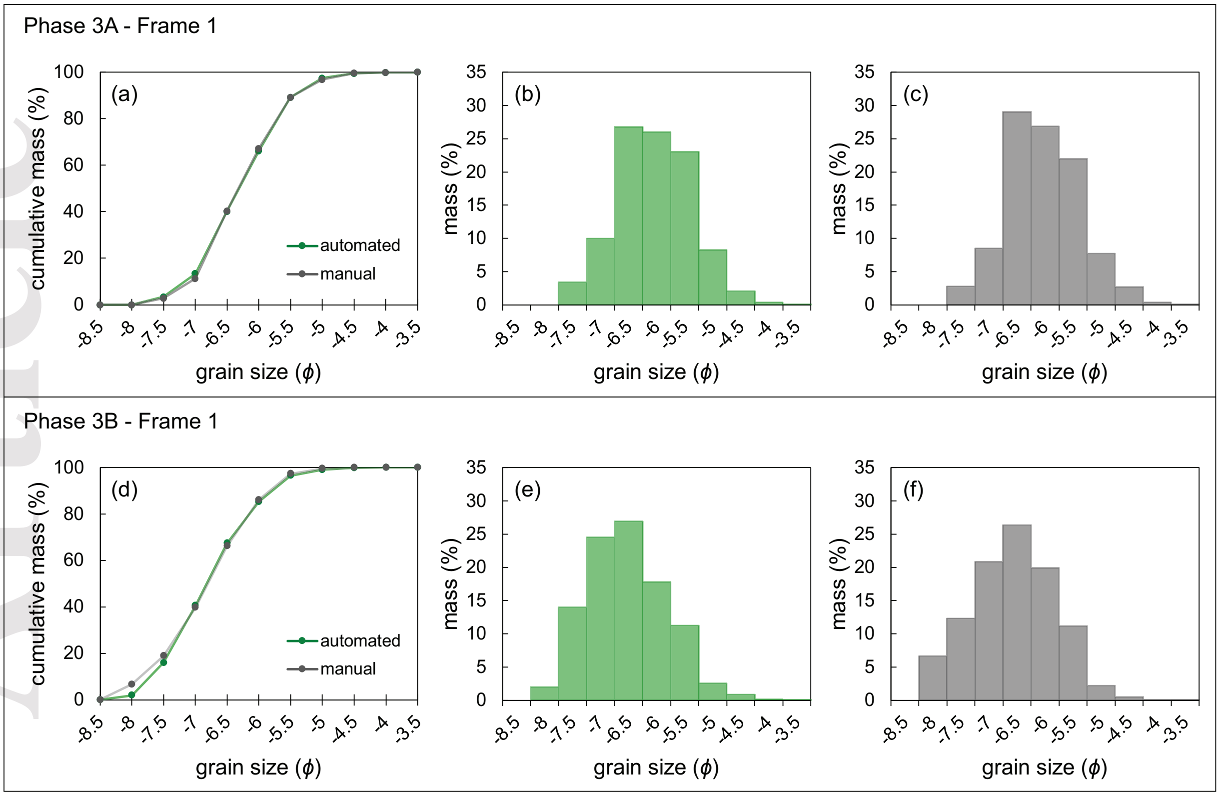
Phase 3A - Frame 1
(a)
(b)
(c)
cumulative mass (%)
mass (%)
automated
manual
grain size (ϕ)
Phase 3B - Frame 1
(d)
(e)
(f)

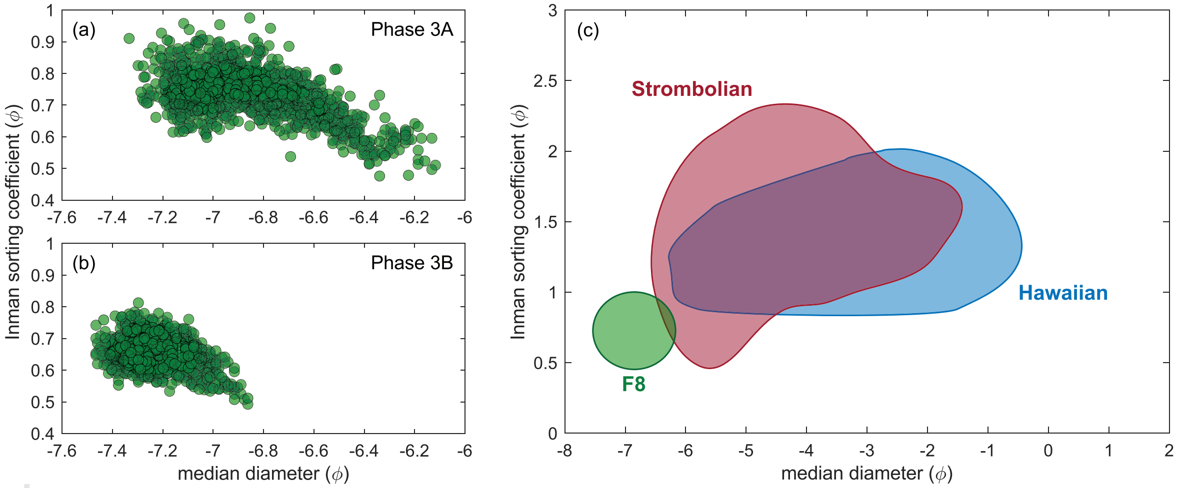
(a)
Phase 3A
(b)
Phase 3B
Inman sorting coefficient (ϕ)
median diameter (ϕ)
(c)
Strombolian
Hawaiian
F8
Inman sorting coefficient (ϕ)
median diameter (ϕ)

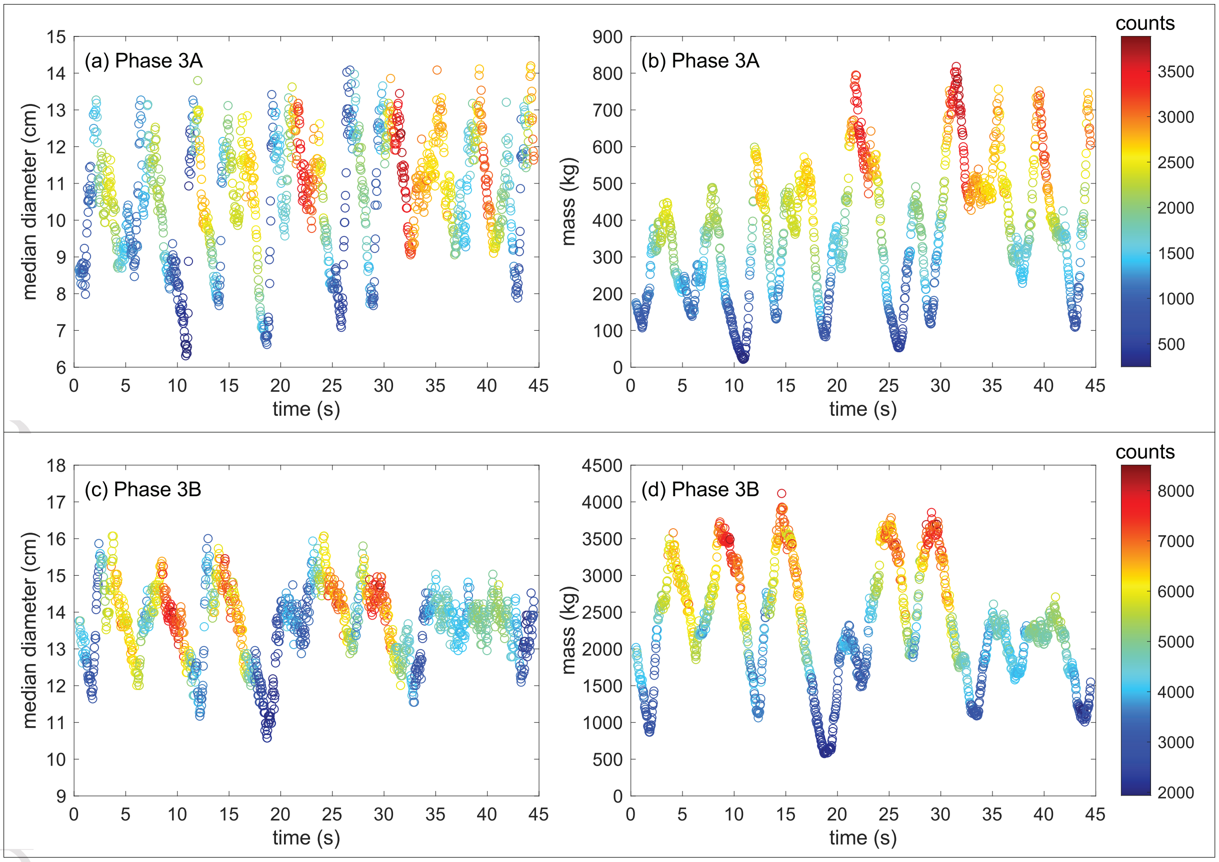
(a) Phase 3A
median diameter (cm)
time (s)
(b) Phase 3A
mass (kg)
time (s)
counts
(c) Phase 3B
median diameter (cm)
time (s)
(d) Phase 3B
mass (kg)
time (s)
counts

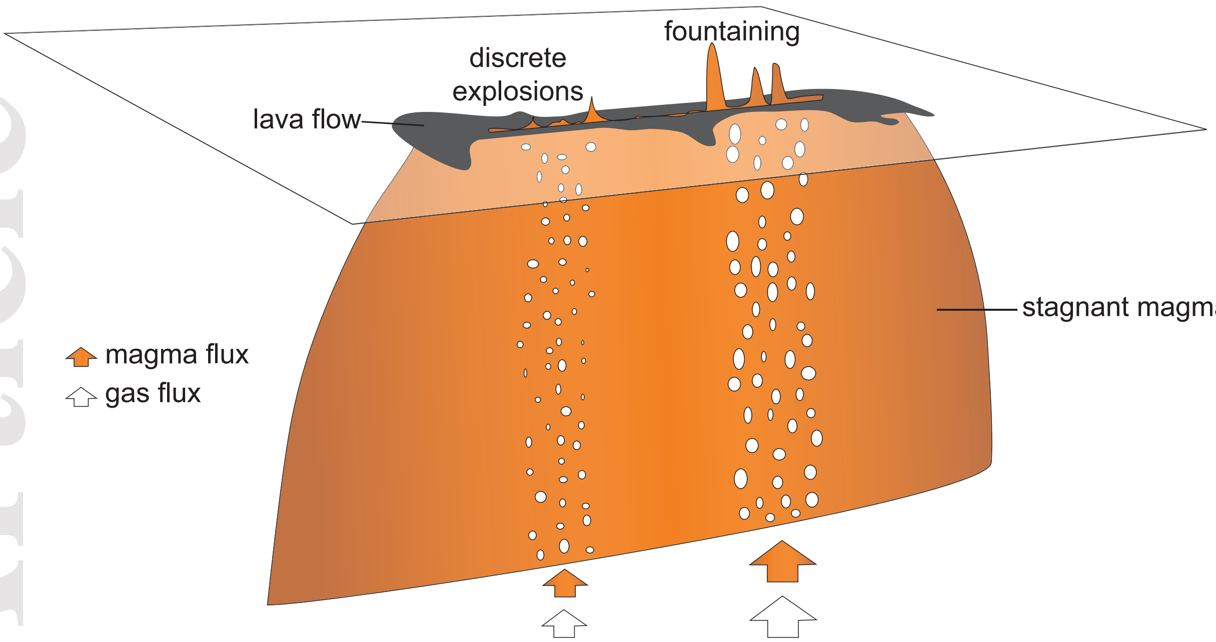
fountaining
discrete explosions
lava flow
stagnant magma
magma flux
gas flux

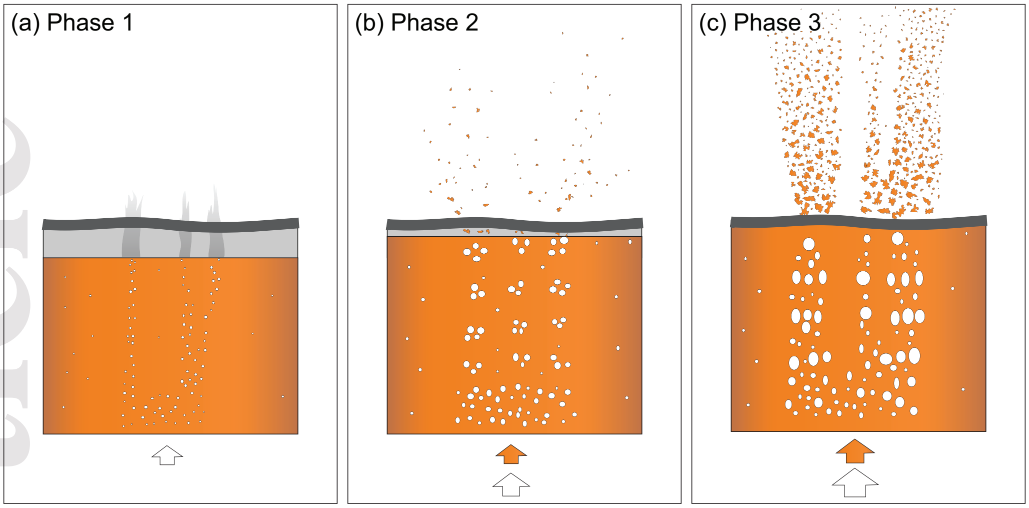
(a) Phase 1
(b) Phase 2
(c) Phase 3